International Journal of Geo-Information

MDPI

Article

OBIA-Based Extraction of Artificial Terrace Damages in the Loess Plateau of China from UAV Photogrammetry

Xuan Fang [1], Jincheng Li [1], Ying Zhu [1], Jianjun Cao [1], Jiaming Na [2,*], Sheng Jiang [3] and Hu Ding [4]

[1] School of Environment Science, Nanjing Xiaozhuang University, Nanjing 211171, China; fangxuan@njxzc.edu.cn (X.F.); 18050105@njxzc.edu.cn (J.L.); 2009007@njxzc.edu.cn (Y.Z.); jjcao@njnu.edu.cn (J.C.)
[2] College of Civil Engineering, Nanjing Forestry University, Nanjing 210037, China
[3] School of Mechatronics and Information, Wuxi Vocational Institute of Arts and Technology, Yixing 214206, China; jiangsheng@wxgyxy.edu.cn
[4] School of Geography, South China Normal University, Guangzhou 510631, China; hu_ding@m.scnu.edu.cn
* Correspondence: jiaming.na@njfu.edu.cn

Abstract: Terraces, which are typical artificial landforms found around world, are of great importance for agricultural production and soil and water conservation. However, due to the lack of maintenance, terrace damages often occur and affect the local flow process, which will influence soil erosion. Automatic high-accuracy mapping of terrace damages is the basis of monitoring and related studies. Researchers have achieved artificial terrace damage mapping mainly via manual field investigation, but an automatic method is still lacking. In this study, given the success of high-resolution unmanned aerial vehicle (UAV) photogrammetry and object-based image analysis (OBIA) for image processing tasks, an integrated framework based on OBIA and UAV photogrammetry is proposed for terrace damage mapping. The Pujiawa terrace in the Loess Plateau of China was selected as the study area. Firstly, the segmentation process was optimised by considering the spectral features and the terrains and corresponding textures obtained from high-resolution images and digital surface models. The feature selection was implemented via correlation analysis, and the optimised segmentation parameter was achieved using the estimation of scale parameter algorithm. Then, a supervised k-nearest neighbourhood classifier was used to identify the terrace damages in the segmented objects, and additional geometric features at the object level were considered for classification. The comparison with the ground truth, as delineated by the image and field survey, showed that proposed classification can be adequately performed. The F-measures of extraction on three terrace damages were 92.07% (terrace sinkhole), 81.95% (ridge sinkhole), and 85.17% (collapse), and the Kappa coefficient was 85.34%. Finally, the potential application and spatial distribution of the terrace damages in this study were determined. We believe that this work can provide a credible framework for mapping terrace damages in the Loess Plateau of China.

Keywords: object-based image analysis (OBIA); terrace damages; Loess Plateau of China; UAV photogrammetry

Citation: Fang, X.; Li, J.; Zhu, Y.; Cao, J.; Na, J.; Jiang, S.; Ding, H. OBIA-Based Extraction of Artificial Terrace Damages in the Loess Plateau of China from UAV Photogrammetry. *ISPRS Int. J. Geo-Inf.* **2021**, *10*, 805. https://doi.org/10.3390/ijgi10120805

Academic Editor: Wolfgang Kainz

Received: 9 October 2021
Accepted: 27 November 2021
Published: 30 November 2021

1. Introduction

Terraces, which are represented by a series of successively receding flat surfaces along contour lines on slopes [1], are typical artificial landforms in hilly and mountainous areas [2]. Terracing can increase arable land and agricultural production [3,4] and contribute to soil and water conservation [5,6] by changing the local topography of slopes and their corresponding water flow process [7] and soil properties [8]. The artificially terraced landscapes that have been developed widely around the world [2,9] can enhance biodiversity and landscape diversity [10,11] and provide aesthetic, cultural, and tourism landscape value [12–14]. However, localised movement and erosion are likely to occur on terraced

fields due to steep ridges, as manifested by the micro-landforms of terrace damages, including collapse and sinkholes [15–18]. Around the world, terrace damages are closely related to farmland abandonment or lack of maintenance [9,17,19–22]. According to the reviewed literature, terrace damage provides a major material source for hydrogeological hazards during intense rainfall [23] and threatens food security and historical landscapes [24,25].

The Loess Plateau of China is one of the areas with the most serious soil erosion in the world due to its broken terrain and loose loess [26]. Terracing has a long history, and the amount of terraces had greatly increased during the second half of the last century. The implementation of transforming slopes into cultivated terraces have helped to overcome poverty [27,28]. Furthermore, terracing is an important strategic measure for soil conservation in the Loess Plateau of China [29,30]. Since the late 1990s, the program called 'Grain for Green' has contributed to the conversion of steep cultivated land into forests and grasslands [31,32], and it has led to the ecological and economic migration of farmers [33–35]. A large number of farmlands, including terraced farmlands, on the Loess Plateau have been abandoned [36]. The improvement of the ecological environment of the Loess Plateau in recent years has proven the success of the 'Grain for Green' program, and it represents an important victory of soil and water conservation via vegetation restoration [26,37,38]. However, the loss of agricultural ecosystem services of the Loess Plateau caused by abandoned farmlands remains to be a concern, as it may threaten food security and rural social development [39].

Our research team conducted the investigation after a serious rainstorm on July 15, 2020 in Suide, Shaanxi, China. Figure 1 shows examples of common problems related to terrace damages. An investigation of terrace damages is extremely important in understanding the processes involved in land degradation. Due to the presence of extremely complex and broken terrains, manual investigation alone is time-consuming, laborious, and dangerous. Moreover, terrace damage is a complex problem because it is influenced by slope gradients and heights of terrace steps, vegetation cover, and time of abandonment [9,40,41]. The efficient and accurate (semi-)automatic exploration of micro-topographical features and corresponding spatial distributions of loess terrace damages is an essential task in understanding the dynamics and trend of terrace degradation and the protection of terraced lands for sustainable ecological services. Therefore, large-scale terrace failure research is necessary to reveal the occurrence mechanism and spatial distribution law of terrace damages.

Figure 1. Terrace damages found by our field investigation. The damages generally include (**a**) collapse; (**b**) terrace sinkhole; and (**c**) ridge sinkhole.

Due to the small size of the micro-landform-scale terrace damages, high-resolution imagery is necessary for terrace damage extraction. The development of unmanned aerial vehicle (UAV) photogrammetry and light detection and ranging (LiDAR) remote sensing can guarantee the data accessibility of high-resolution images. Unlike satellite-based sensors, both aforementioned approaches can create high-resolution topographical data and orthophoto images [42] and simultaneously realise field survey and remote sensing [43,44]. Amongst both approaches, UAV photogrammetry is more flexible and entails a lower cost compared with LiDAR [45]. The recent studies about terraces degradation have

also shown that UAV photogrammetry is effective for damage identification and erosion evaluation [46]. The monitoring of terrace damages in these previous studies was achieved via accurate terrain modelling. Since the terraces are always covered by dense vegetation, the terrain model task should firstly remove all the vegetation points from the digital surface model (DSM) generated by UAV photogrammetry. This could be achieved by some proposed automatic filtering algorithm, which is mainly based on local surface filtering [47,48]. However, the recurrent filtering algorithm for generating DEM is mainly suitable for flat areas but not for the Loess Plateau with broken terrain [49]. Therefore, it is necessary to explore the method of extracting terrace damages directly from DSMs and images generated by UAV photogrammetry.

Object-based image analysis (OBIA) is a relatively new remote sensing image processing approach with respect to the traditional pixel-based one. OBIA performs segmentation via a clustering method to determine the pixel groups belonging to a single meaningful object and then classifies the segmented objects [50]. Compared with pixel-based methods that do not use spatial concepts [51], the object-based method is more advanced, as it exploits the spatial information of target features, such as spectral, shape, and textural features [52–56]. Moreover, owing to the use of high-resolution data with high spectral variety between pixels, which often results in oversampling, the approach of OBIA of clustering pixels into objects is more effective than that of the pixel-based method [57] in processing high-resolution images requiring terrace damage extraction. The recent studies have also proven that OBIA and UAV data can be successfully applied in many fields, such as building safety [58–61], crop production [62,63], landslide movement [64,65], and artificial terrace mapping [52,66].

Inspired by the above considerations, the present work focuses on the extraction of terrace damages. The objective of this study is to propose an OBIA workflow for the automatic extraction of terrace damages in the Loess Plateau of China. The proposed workflow is based on high-resolution imagery and digital surface model (DSM) from UAV photogrammetry.

2. Materials and Methods

2.1. Study Area

A terraced slope called Pujiawa (110°21′21″ E–110°21′32″ E, 37°34′18″ N–36°34′32″ N) was selected as the study area (Figure 2a,b). It is located in the Jiuyuangou catchment, Suide County, Shaanxi Province, China. The Jiuyuangou catchment is in a loess hilly and gully area of the Loess Plateau, where terracing is widespread as an important measure for soil and water conservation since the 1950s [52]. The climate is semi-humid with an average annual temperature of 8 °C and an average precipitation of 475.1 mm. Most of the annual precipitation is concentrated between June to September in the form of high-intensive precipitation that can cause severe soil erosion [67]. The study area has an elevation range of 1034.6–1143.9 m and an area of 8.102 ha. There are narrow man-made terraces in the north with a field width of about 3–6 m and wide machine-made terraces in other areas with a field width of about 10–30 m. The 'Grain for Green' program here was started in 1999. Most terraced farmlands had been converted into grasslands. The vegetation cover was first planted with artificial alfalfa in response to the 'Grain for Green' program and then was naturally restored due to no manual management. Moreover, the lack of manual maintenance had led to the frequent occurrence of terrace damages. At present, Pujiawa terraces have been abandoned for more than 20 years, and the terraces are obviously damaged, which is manifested in multiple collapses and sinkholes.

2.2. Data Acquisition

High-resolution orthophoto imagery and the corresponding DSMs were used to extract the terrace damages. Images with a ground sample distance of 3 cm was generated using UAV photogrammetry in August 2020 (Figure 2c,d). Two main phases, namely, outdoor field survey and subsequent indoor image processing, were included in the data

generation. For the outdoor survey, a DJI Phantom 4 RTK drone was firstly used to capture the optical aerial photographs of the study area with WGS-84 coordinates. This drone system equipped RGB camera (5472 × 3648 resolution and 24 mm focal length) and Real-Time Kinematic (RTK) receivers with 1.5 cm vertical and 1 cm horizontal measurement accuracy. A total of 218 images were generated with a 70% flight overlapping rate and a 50% side overlapping rate. Secondly, the horizontal and vertical accuracies were maintained on the basis of 15 check points (CPs) obtained via Post-Processed Kinematic (PPK) GNSS measurements. The indoor image processing was mainly implemented in two steps, namely, data generation and ground truth generation. The Pix4D Mapper software was used for data generation. Aerial triangulation was initially performed on the basis of the bundle block adjustment. A total of 2,697,507 3D key points were eventually matched with the overlapped images. Subsequently, the dense point cloud was generated from the 3D triangulation network and then rasterised into an image and a DSM. According to the accuracy assessment with CPs, the root square mean error (RSME) of the final DSM was 0.075 m. Then, ground truth generation was performed by manually interpreting the generated image. Reference polygons (Figure 2d) were manually delineated from both the field investigation and the details of the terrace based on the generated data.

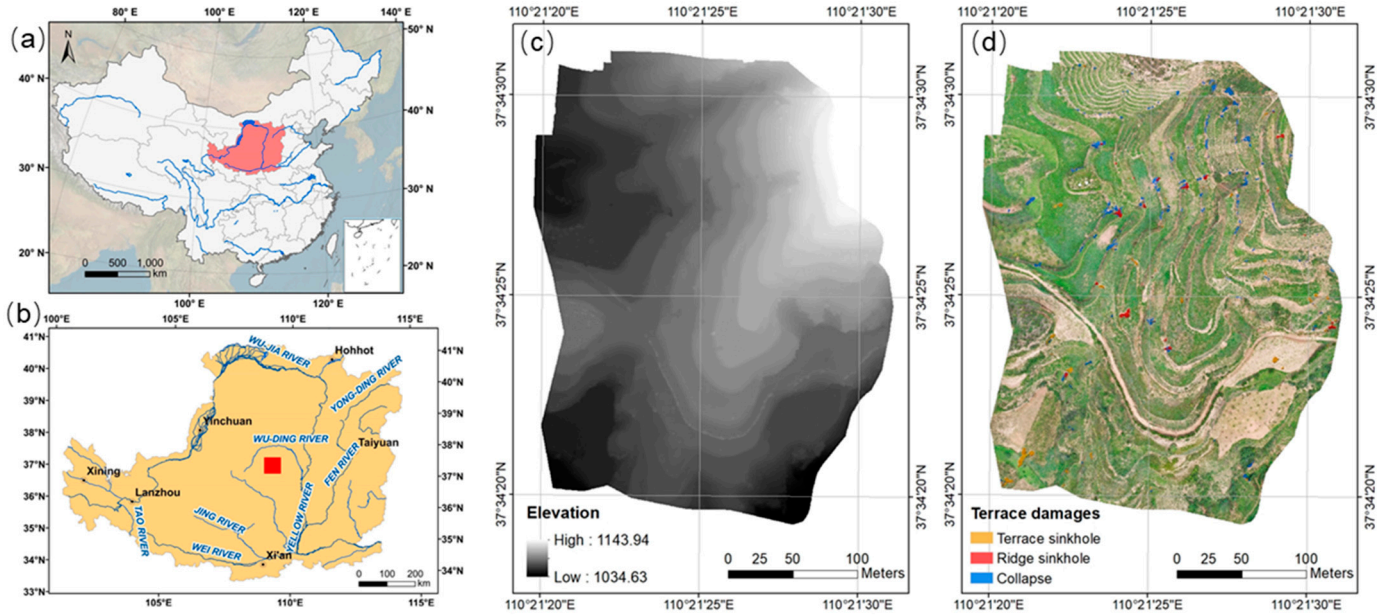

Figure 2. Study area and data: (**a**,**b**) Locations of the Loess Plateau, China and the study area; (**c**) DSM of the study area obtained from UAV photogrammetry; (**d**) Image obtained from UAV photogrammetry with reference polygons of terrace damages by artificial interpretation.

2.3. OBIA-Based Terrace Damage Extraction

The mapping task was started with image segmentation, which is an essential step that can affect the final mapping accuracy. Multiple resolution segmentation (MRS) [51,68] was utilised in this study. The spectra and topographies and their corresponding textures were used as the features for segmentation as a means of achieving the best result. Optical feature selection was conducted via correlation analysis, and the Estimation of Scale Parameter (ESP) Tool [69] was used to optimise the segmentation parameters. Subsequently, a supervised classification strategy based on the k-nearest neighbour (kNN) was performed to identify the terrace damages, including the collapse and sinkholes. The spectrum and topography and their corresponding textures and the geometry of each segment were calculated as the features for classification. Then, the sinkholes were classified into two types, namely, ridge sinkhole and terrace sinkhole, by using a local terrain feature derived

from the DSM. Finally, the mapping results were validated and compared via an accuracy assessment analysis. Figure 3 illustrates the entire workflow of this study.

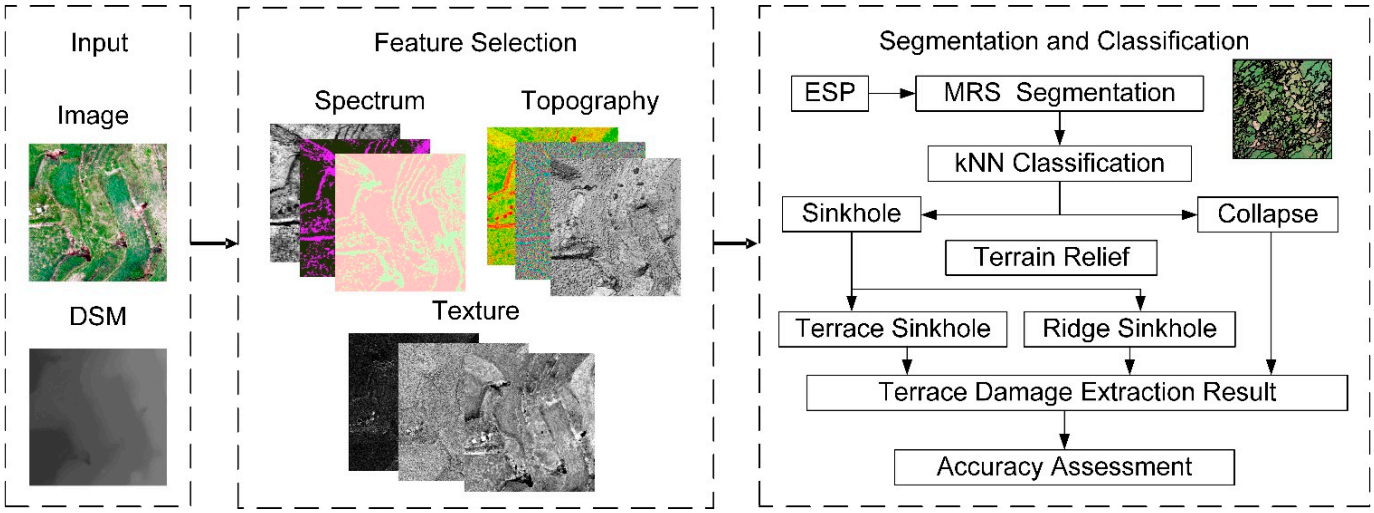

Figure 3. Workflow of the proposed extraction method.

2.3.1. Image Segmentation

The commonly used MRS for images integrated in the eCognition software was implemented in this study. In MRS, an appropriate feature combination and optimal segmentation parameters should be selected. Then, segments are used as the basic processing units for terrace mapping.

(1) Feature selection

Twenty-three features, including the spectra and topographies and their corresponding textures, were considered for object segmentation in this study. An overview of these features and the detailed description for each feature are listed in Table 1. As spectral and topographic features are widely used in the OBIA community [56,66,70,71], this information was firstly considered. For the spectral features, the R, G, and B bands from the images and a vegetation index based on the above-mentioned three features called EXG were considered. Three basic topographic factors, namely, elevation, hill shade, and slope, were utilised. The spectral and topographic textures, which are beneficial for extracting landform entities [72,73], were also adopted. Four terrain texture measures derived from the grey-level co-occurrence matrix (GLCM) [74] were calculated on the basis of all seven spectral and topographic features.

Pre-selected features can express characteristic and spatial features from different perspectives. However, each pair of factors may also have high correlation, and it can introduce overlapping and redundant information. Thus, the pre-selected features should be optimised to reduce the time complexity of the segmentation process. Correlation analysis was used in cases in which a subset of lower-correlation features (coefficients less than 0.5) needed to be selected from 23 preselected features.

(2) Segmentation parametric optimisation

MRS is a bottom–up region-based approach that begins with one pixel and merges the neighbouring pixels with minimum heterogeneity increment until the heterogeneity of the object exceeds a certain user-defined threshold. Recent studies have emphasised that certain segmentation parameters, particularly scale, shape, and compactness, will strongly affect the segmentation. Given that optimising the segmentation parameters typically rely on subjective trial-and-error methods, many studies have focused on automatic scale optimisation methods. ESP version 2.0 [69] is widely adopted for exploring the scale

parameter [77–79]. Subsequently, the optimal shape and compactness parameters based on the heterogeneity criterion have been utilised [42,55], as shown in the literature review.

Table 1. Overview of the features used for segmentation.

Type	Features	Abbreviation	Description
Spectrum	Red	R	The intensity value of the pixel within red, green, and blue bands, respectively.
	Green	G	
	Blue	B	
	EXG	EXG	Excess green index by Woebbecke (1995) [75] provided a near-binary intensity image outlining a plant region of interest, which has been widely cited and used in recent UAV photogrammetry based studies: $EXG = 2G - R - B$, where R, G, and B stand for the intensity value of the pixel within red, green, and blue bands, respectively.
Topography	Elevation	Ele	Original height from the DSM.
	Hillshade	HSh	The simulation of a light source in a certain direction and a certain height of the sun [76].
	Slope	Slp	The tangent of the angle of that surface to the horizontal terrain [76].
GLCM Texture	Homogeneity	Homo	The GLCM measures how often different combinations of pixel grey levels occur in a scene. In this study, the terrain texture features were derived from GLCM based on five topographic layers. The detail for calculating GLCM was taken from the study by Haralick et al. (1973) [74].
	Entropy	Ent	
	Mean	Mean	
	Correlation	Cor	

2.3.2. Terrace Damage Classification

After achieving the optimal segmentation, the segment is classified via supervised classification. K nearest neighborhood (kNN) classification, a powerful tool used in many object-based procedures [80,81] because of its flexibility and simplicity, can be used for terrace damage mapping. However, certain features need to be determined to train the classifiers. As the generated segments require additional geometry information compared with the pixel-level image, all features to be used in classification require object-level calculation. Then, the combined features can be optimised via importance ranking. In this study, kNN was adopted using the eCognition software (Trimble Geospatial, Munich, Germany).

After performing kNN classification, the original segments are classified into three types: namely, collapse, sinkholes, and others. As a means of differentiating the sinkholes into subtypes (i.e., ridge and terrace) of terrain features, the terrain relief is introduced to the next-level classification. Terrain relief can be defined as the difference between the maximum and minimum elevations within a given area [82]. Considering that there would be a huge difference near the ridges for terrain relief, the sinkholes could be classified by a threshold. Field investigation indicates that terrace ridges in study area are normally higher than 0.5 m, therefore, it can be used for this threshold. The average terrain relief of terrain sinkhole classification result by kNN will be firstly calculated based on original DSM and then classified into two sub-types.

2.3.3. Accuracy Assessment

After completing the extraction of terrace damages, the predicted results can be validated on the basis of the reference data. In this study, the F1-score (*F1*) and Kappa

coefficient (k) were adopted in the accuracy assessment. These metrics can be calculated as follows:

$$F1 = \frac{2 \times Pr \times Re}{Pr + Re}, \text{ where } Pr = \frac{TP}{TP + FP} \text{ and } Re = \frac{TP}{TP + FN} \quad (1)$$

$$k = \frac{P_0 - P_e}{1 - P_e}, \text{ where } P_0 = \frac{TP + TN}{TP + FP + TN + FN} \text{ and } P_e = \frac{(TP + FP)(TP + FN) + (FN + TN)(TN + FP)}{(TP + FP + TN + FN)^2} \quad (2)$$

where TP, FP, TN, and FN denote the true positive, false positive, true negative, and false negative amount with respect to the reference, respectively.

3. Results

3.1. Segmentation Results

3.1.1. Feature Selection Result from Correlation Analysis

The correlation of the pre-selected features for segmentation was calculated firstly. The results are presented in Appendix A. Then, the high-correlation features were removed to reduce the time complexity during segmentation. From the table, we can see that EXG has a strong correlation with R and B; thus, it was removed, and we kept R, G, and B. A similar situation also occurs for GLCM textures of R and B; therefore, they are all removed. As for GLCM textures of G, we kept G_Mean and G_Cor for segmentation due to their lower correlation to other features. For terrain texture features, we kept Ele_Cor for the same reason. Finally, eight remaining features, namely, R, G, B, G_Mean, G_Cor, Ele, HSh, and Ele_Cor were selected for the next step of MRS.

3.1.2. Segmentation Parametric Optimisation Result by ESP

A preliminary experiment shows that range scale of 20 to 100 was close to the actual boundaries of the terrace damage. Hence, this range was considered to be a reasonable scale. Then, ESP was performed to obtain the best scale factor (Figure 4). On the basis of the optimal shape and compactness values and the range of a reasonable segmentation scale, the optimal segmentation scale was estimated using the ESP tools. Figure 4 shows that the four best scale parameters are 66, 79, 92, and 98 because their rates of changes achieve a local peak.

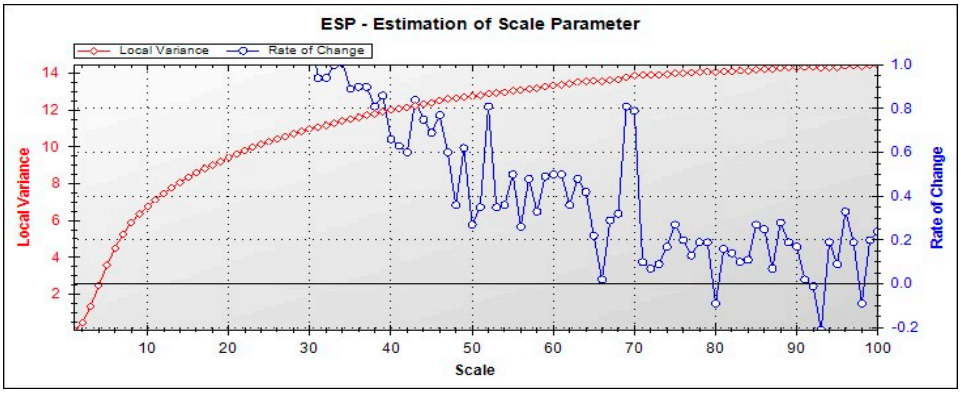

Figure 4. ESP result.

Then, four candidate scales were used for segmentation (Figure 5). Then, the scale of 98 was considered to be the optimal scale as a means of overcoming the problem of over-segmentation. Given a fixed scale of 98, different shape and compactness values were tested. The optimal shape and compactness values were 0.1 and 0.5, respectively.

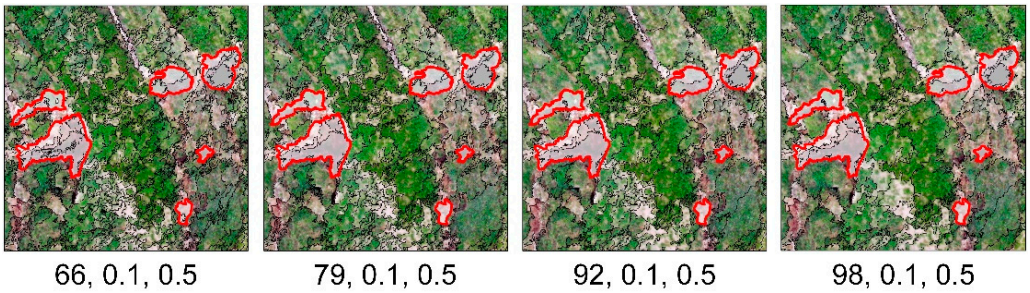

Figure 5. Segmentation results with different candidate scale parameters. The three values under each figure represent the scale, shape, and compactness, respectively. The actual terrace damage areas are highlighted by red lines.

3.1.3. Final Segmentation Results by MRS

The original image was finally segmented into objects by MRS using the selected feature combination and the optimal parameters. A total of 16,838 objects were generated in the segmentation process.

3.2. Classification Results

3.2.1. Feature Selection Result via Importance Ranking

An overview of the features for classification and the detailed descriptions of each feature are shown in Table 2.

Table 2. Overview of the features used for terrace damages classification.

Type	Features (Abb.)	Description
Spectrum (4)	EXG	The mean intensity (_Mean) and standard deviation (_Std) of all pixels forming an image object within each band calculated by Table 1, $\overline{C} = \frac{1}{n}\sum_{i=1}^{n} C_i$ where C_i denotes the intensity value at the pixel in an image object; and n is the total number of an object.
	MaxDiff	Spectrum difference of all layers, $MaxDiff = \frac{\lvert\overline{C_i}(k)-\overline{C_j}(k)\rvert}{B(k)}$ where i, j are image layers; $B(v)$ is the brightness of the image object k; $\overline{C_i}(k)$ is the mean intensity of image layer i of image object k; and $\overline{C_j}(k)$ is the mean intensity of image layer j of image object k.
	Brg	The mean value of the $\overline{C}$ of all layers, $B = \frac{1}{n_L}\sum_{i=1}^{n_l} \overline{C_i}$ where C_i denotes the mean intensity value of layer i; and n_L is the total number of layers.
Topography (6)	Ele	The mean intensity (_Mean) and standard deviation (_Std) of all pixels forming an image object within elevation and hillshade.
	HSh	
	Slp	
GLCM Texture (6)	G_Mean	The mean intensity (_Mean) and standard deviation (_Std) of all pixels forming an image object within each feature calculated by the Table 1.
	G_Cor	
	Ele_Cor	

Table 2. *Cont.*

Type	Features (Abb.)	Description
Geometry (3)	PA	The number of pixels forming an image object.
	LW	A length-to-width ratio of an image object, $r = \frac{a^2+\left[(1-f)b^2\right]^2}{P_k}$ where $f = \frac{P_k}{ab}$; a and b are the length and width of the bounding box of the image object k. P_k is the total number of pixels contained in object k.
	Shp	Shape index is the smoothness of an image object border, $SI = \frac{b_k}{4\sqrt{P_k}}$ where b_k is the border length of an image object k, which is defined as the sum of the edges of the object k. P_k is the total number of pixels contained in object k. The smoother the border of an image object, the lower its shape index.

The variable importance was assessed on the basis of the separation distance of the standard nearest neighbour feature space. An optimal feature subset for classification could be selected when feature combination achieves the maximum average distance in the feature space. Then, this feature combination will be used to generate the kNN classification model. As shown in Figure 6, the first 12 features amongst the total 19 features have a strong influence on accurate classification, namely G_Mean_Mean, G_Mean_Std, G_Cor_Mean, Ele_Cor_Std, EXG_Std, Maxdiff, Brg, G_Cor_Std, Hsh_Mean, Ele_Cor_Mean, EXG_Mean, and Shp. Therefore, the top 12 features were used to construct the kNN classifier.

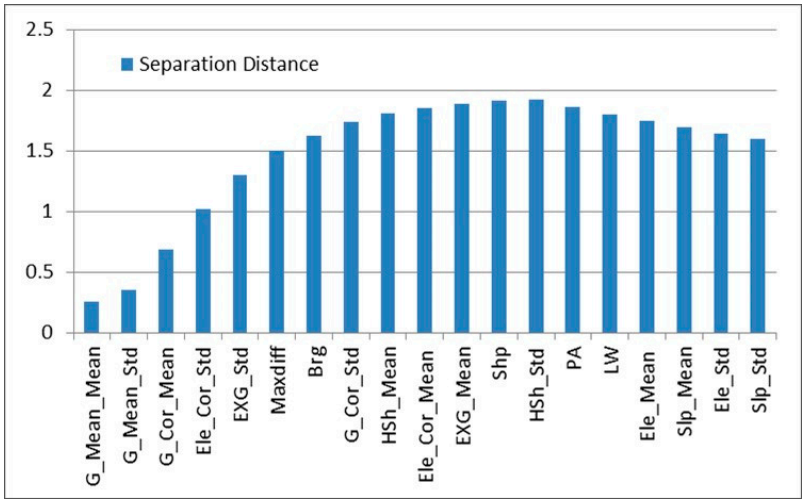

Figure 6. Feature ranking for kNN classification.

3.2.2. Classification Result by kNN

Some samples from the segments were randomly and manually chosen as the training samples based on the images. The same number of training samples for each terrace damage type was ensured. Then, the remaining objects were used for kNN classification, after which twelve features (see Section 3.2.1) were selected for classification by considering the variable importance ranks. Then, the obtained sinkholes from the kNN classification results were classified into two subtypes by using the train relief. The final classification result is illustrated in Figure 7.

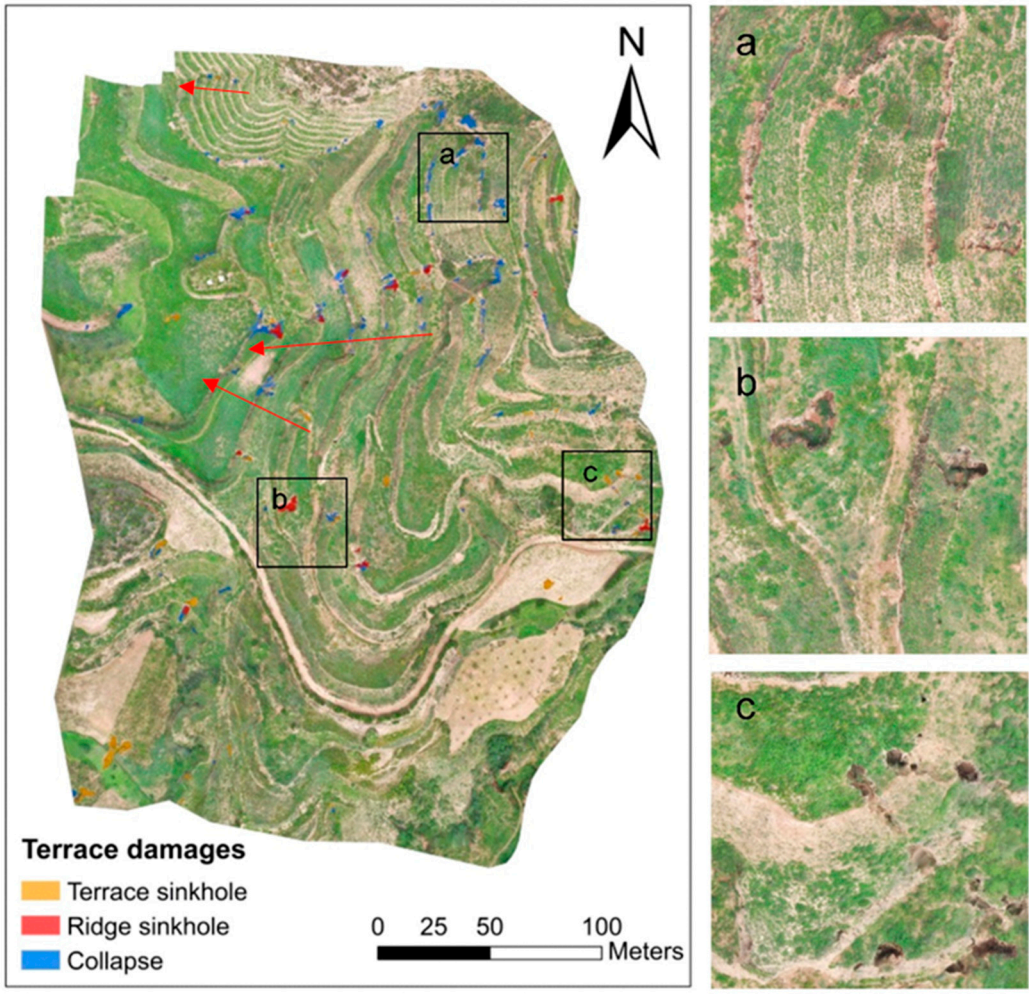

Figure 7. Classification result. The left figure is the classification map of terrace damages, and the three figures on the right show the images without overlapping classification results within the box area of the left figure. The red arrow shows the terrace damages are continuously distributed along the slope.

3.3. Accuracy Assessment Result

Table 3 summarises the per-pixel confusion matrix and accuracy assessment statistics with respect to the reference. The F-measure values of the three extracted terrace damages were 92.07% (terrace sinkhole), 81.95% (ridge sinkhole), and 85.17% (collapse), and the Kappa coefficient was 85.34%. The results indicate that most of the damages of the total areas had been correctly classified.

Table 3. Confusion matrix between classification result and ground truth (area: m^2).

	Actual Terrace Sinkhole	Actual Ridge Sinkhole	Actual Collapse	Actual Other	Total
Predicted Terrace Sinkhole	227.29	0	5.46	18.24	250.99
Predicted Ridge Sinkhole	1.99	118.25	1.25	7.52	129.01
Predicted Collapse	14.9	1.53	472.12	100.45	589
Predicted Other	38.56	8.09	84.39	79,921.47	80,052.51
Total	282.74	127.87	563.22	80,047.68	81,021.51

4. Discussion

4.1. Rationality of the Proposed Method

The automatic classification method based on the high-resolution imagery and topographic data, which can reflect the characteristics of the surface material, coverage, and terrain, is a promising approach for monitoring various surface changes in ecology [83], mountain disaster [84], and geomorphology [85]. OBIA, an automatic classification method, has been proven to be efficient in mining image information and terrain data [86]. The surface coverage of terrace area is characterised by regular stepped distribution due to its stepped terrain, but terrace damages characterised as irregular micro-landforms (such as collapse and sinkhole) break this regularity. On the basis of our understanding of the actual characteristics of degraded terraces, we proposed a hypothesis that the damaged and the non-damaged parts can be distinguished using topographic, spectral, and textural features. Based on the hypothesis, our method was implemented using terrain indexes, GLCM textures, and spectral response during terrace damages extraction. The results of our study confirmed that the object-oriented method can effectively extract terrace damages with a Kappa coefficient of 85.34%. Not only the spatial distribution of the terrace damages but also the different types of damages can be classified with high accuracy.

The research on monitoring terrace degradation has shown that DEM via UAV photogrammetry can effectively map terrace damages, contributing to flow simulation and calculation of erosion amount [46]. Unlike DEM, DSM includes vegetation elevation information. However, the production of DEMs by removing the vegetation point from DSM is time-consuming and not suitable for the Loess Plateau with broken terrain [47–49]. In addition, the study area is mainly covered by grassland. Therefore, the selection of experimental data is reasonable, and this study realised the extraction of terrace damages based on DSMs and images without DEMs.

4.2. Spatial Distribution of Terrace Damages

The research on the spatial distribution of terrace damages needs high-precision surface data or field investigation to obtain the micro-geomorphic change on terraced slope [46]. Therefore, the literature regarding terrace damages was mostly conducted at the slope scale [41,46]. Factors that could affect the damage distribution of terraces include the abandonment age, vegetation cover, and topography of slopes where terraces are located [9,40,41].

Our research was implemented on a horizontal terrace in a slope-scale area. The results depict two obvious characteristics for the spatial distribution of terrace damages on the studied slope. Firstly, the number and area of the terrace damages on the terraces with low ridges and narrow fields in the north are significantly less than those with high ridges and wide fields (Figure 7). Terracing could reduce the outflow volume by intercepting runoff, altering the path of runoff and decreasing the hydrological connectivity, thus encouraging infiltration [86,87]. Compared with narrow terraces, wide terraces have more infiltration water and can more easily form sinkholes. Consequently, more water volume increases the gravity of the terrace, hence the high likelihood of collapse. Our finding is consistent with the research on rice terrace research, which showed that too much water by irrigation would cause a collapse [88]. Secondly, the damage of terraces tends to be continuously distributed along the slope indicated by the red arrow in Figure 7, reflecting the influence of the water output of the upper step on the downer step. In the slope-scale area, the climate, soil, vegetation cover, and abandoned time conditions are consistent. Our study indicated that the occurrence of terrace damages is related to the morphological characteristics of terraces, including the height of the steps, the width of the field surface, and the number of steps.

4.3. Potential Application

Terrace damage extraction is the basis for knowing the spatial distribution and temporal evolution of terrace damages. Targeted measures for terrace management and construction can also be determined on the basis of the type, degree, and impact mech-

anism of the terrace damages. This study is a meaningful work for finding the precise location, size, shape, and spatial patterns of terrace damages.

The proposed method has been implemented via experiment on horizontal terraces whose area accounts for 54% of the terraces on the Loess Plateau of China [89]. Firstly, although this study area is small, the terraces have different field widths and ridge heights. It indicated the effectiveness of this method is not affected by the shape and size of terraces. Secondly, the method can extract collapse and sinkhole damages, which are two typical manifestations of terrace failure in the Loess Plateau of China [90]. Thirdly, good extraction results can be obtained based on DSMs and images. It is related to the fact that the study area is basically covered with grass. If there are many trees in the study area, the use of DEMs is recommended to eliminate the impact of vegetation on a real terrain [49]. Therefore, the proposed method has application potential in the damage extraction of horizontal terraces covered grasslands or bare lands. When the study area includes terracing area and non-terracing area, a two-step scheme can be adopted: firstly, extracting the terrace area via the terrace extraction method [52,66], and secondly, using the proposed method for extracting damages in the terrace area.

The specific classification features and rules of this research method are difficult to be directly applied to terraces with different topographic features, such as slope terraces and reverse slope terraces, which is primarily a challenging task, and thus needs further exploration. However, the object-oriented method can flexibly change the classification rules by changing the input classification features according to the actual terrace shape and terrain. In addition, the object-based method is a semi-automatic method by a supervised classifier; unsupervised classifiers may help to realise fully automatic classification. In general, we are optimistic about applying our method in terrace damages extraction.

5. Conclusions

Artificial terraces are common around the world, and they are of great importance in food production, water and soil conservation, and ecological protection. The problem of terrace damages caused by the lack of manual maintenance has drawn increasing attention, but an automatic mapping method is still lacking. Recent technological development of UAV photogrammetry and the good performance of OBIA for high-resolution image processing tasks have application potential in terrace damage extraction. In this study, we explored the potential of the OBIA framework based on UAV photogrammetry for terrace damage mapping. We conducted experiments on an area of the Loess Plateau, China by using aerial imagery with 3 cm resolution and DSM from UAV photogrammetry. The feature selection, segmentation parametric optimisation, and classification tasks were optimised by considering the specific task objectives. Our results indicate that the proposed method can obtain acceptable and accurate classification results. However, the OBIA framework for terrace damage mapping can still be improved. Other types of data sources, such as LiDAR data, may help to enhance the OBIA framework. Unsupervised classifiers may be introduced to simplify the whole process. This suggested approach will require several in-depth studies in the future.

Author Contributions: Conceptualisation: X.F.; methodology: X.F. and J.N.; software: J.L.; validation: X.F. and J.L.; formal analysis: X.F. and J.N.; writing—original draft preparation: X.F. and J.N.; writing—review and editing: X.F., J.N., Y.Z. and S.J.; visualisation: J.L., J.C. and H.D.; funding acquisition: X.F. and J.N. All authors have read and agreed to the published version of the manuscript.

Funding: This work was financially supported by the Natural Science Foundation of China (Nos. 41871313, 42001329 and 41771415), the Natural Science Foundation of Jiangsu Province (No. BK20161118 and BK20201121), and Key Laboratory for Digital Land and Resources of Jiangxi Province, East China University of Technology (DLLJ202101).

Data Availability Statement: Data from this research will be available upon request to the authors.

Conflicts of Interest: The authors declare no conflict of interest.

Appendix A

The detailed feature correlation matrix used for segmentation in this study.

Table A1. Correlation matrix of pre-selected features for segmentation.

Features	R	G	B	EXG	R_Mean	R_Homo	R_Ent	R_Cor	G_Mean	G_Homo	G_Ent	G_Cor	B_Mean	B_Homo	B_Ent	B_Cor	Ele	HSh	Slp	Ele_Mean	Ele_Homo	Ele_Ent	Ele_Cor
R	1.0000																						
G	0.8751	1.0000																					
B	0.9550	0.8714	1.0000																				
EXG	−0.6013	−0.2597	−0.6002	1.0000																			
R_Mean	0.4950	0.4307	0.4720	0.1601	1.0000																		
R_Homo	0.0335	0.0630	0.0511	−0.3522	−0.5707	1.0000																	
R_Ent	−0.0370	−0.0491	−0.0498	0.4639	0.7197	−0.8379	1.0000																
R_Cor	0.0586	0.0574	0.0455	−0.2558	−0.3576	0.3233	−0.4008	1.0000															
G_Mean	0.2987	0.3394	0.2967	0.4081	0.9641	−0.6144	0.7824	−0.3991	1.0000														
G_Homo	0.0596	0.0855	0.0626	−0.3501	−0.5455	0.8984	−0.7980	0.3468	−0.5935	1.0000													
G_Ent	−0.0507	−0.0610	−0.0539	0.4568	0.6992	−0.8038	0.9290	−0.4019	0.7635	−0.8404	1.0000												
G_Cor	0.0471	0.0483	0.0441	−0.2659	−0.3805	0.3426	−0.4206	0.7816	−0.4209	0.3667	−0.4295	1.0000											
B_Mean	0.5126	0.4644	0.5357	0.1216	0.9869	−0.5429	0.6900	−0.3507	0.9521	−0.5249	0.6745	−0.3683	1.0000										
B_Homo	−0.0453	−0.0135	−0.0301	−0.3072	−0.6066	0.9309	−0.8098	0.3126	−0.6370	0.8965	−0.8008	0.3385	−0.5836	1.0000									
B_Ent	0.0179	0.0038	0.0068	0.4316	0.7437	−0.8122	0.9423	−0.3868	0.7970	−0.7964	0.9273	−0.4173	0.7173	−0.8379	1.0000								
B_Cor	0.0889	0.0859	0.0782	−0.2775	−0.3471	0.3212	−0.3973	0.8321	−0.3943	0.3519	−0.4083	0.7861	−0.3376	0.3290	−0.4059	1.0000							
Ele	0.1385	0.0850	0.1195	−0.1186	0.0697	−0.1873	0.1473	−0.0920	0.0296	−0.1938	0.1559	−0.1036	0.0653	−0.2001	0.1587	−0.0939	1.0000						
HSh	0.0336	0.0590	0.0322	−0.0985	−0.1724	0.1667	−0.1915	0.1290	−0.1843	0.1518	−0.1803	0.1336	−0.1663	0.1578	−0.1836	0.1294	0.0141	1.0000					
Slp	−0.2371	−0.3290	−0.2297	−0.0080	−0.1187	−0.0787	0.0474	−0.1261	−0.1142	−0.0833	0.0484	−0.1184	−0.1248	−0.0437	0.0234	−0.1337	0.0230	−0.4410	1.0000				
Ele_Mean	0.0063	0.0039	0.0055	0.5245	0.8701	−0.6847	0.8564	−0.4501	0.9402	−0.6711	0.8411	−0.4702	0.8450	−0.6812	0.8529	−0.4556	0.0452	−0.2171	0.0012	1.0000			
Ele_Homo	0.0134	0.0212	0.0106	0.0195	0.0292	0.0670	0.0093	0.0570	0.0317	0.0711	0.0081	0.0532	0.0276	0.0653	0.0104	0.0557	0.0024	0.0347	−0.0542	0.0260	1.0000		
Ele_Ent	−0.0252	−0.0407	−0.0199	0.0029	0.0113	−0.0507	0.0443	−0.0480	0.0117	−0.0514	0.0452	−0.0450	0.0124	−0.0453	0.0418	−0.0473	−0.0035	−0.0706	0.1109	0.0274	−0.5416	1.0000	
Ele_Cor	0.0253	0.0392	0.0202	0.0019	0.0007	0.0644	−0.0295	0.0622	0.0006	0.0663	−0.0308	0.0580	−0.0007	0.0595	−0.0273	0.0608	0.0056	0.0588	−0.1039	−0.0136	0.7102	−0.7954	1.0000

References

1. Li, X.; Yang, J.; Zhao, C.; Wang, B. Runoff and sediment from orchard terraces in southeastern China. *Land Degrad. Dev.* **2014**, *25*, 184–192. [CrossRef]
2. Socci, P.; Errico, A.; Castelli, G.; Penna, D.; Preti, F. Terracing: From agriculture to multiple ecosystem services. In *Oxford Research Encyclopedia of Environmental Science*; Oxford University Press: Oxford, UK, 2019.
3. Cao, Y.; Wu, Y.; Zhang, Y.; Tian, J. Landscape pattern and sustainability of a 1300-year-old agricultural landscape in subtropical mountain areas, Southwestern China. *Int. J. Sustain. Dev. World Ecol.* **2013**, *20*, 349–357. [CrossRef]
4. Wickama, J.; Okoba, B.; Sterk, G. Effectiveness of sustainable land management measures in West Usambara highlands, Tanzania. *Catena* **2014**, *118*, 91–102. [CrossRef]
5. Dorren, L.; Rey, F. A review of the effect of terracing on erosion. In Proceedings of the Briefing Papers of the 2nd SCAPE Workshop, Cinque Terre, Italy, 13–15 April 2004; pp. 97–108.
6. Qiu, Y.; Xu, M.-x.; Shi, C.-d.; Zhang, Z.; Zhang, S. Dynamic accumulation of soil organic carbon of terrace changed from slope cropland in the hilly loess plateau of eastern Gansu Province. *J. Plant Nutr. Fertil.* **2014**, *20*, 87.
7. Wang, P.; Wang, K.; Li, T.; Li, Y. Regulation effects of reverse-slope level terrace on the runoff and sediment yield in sloping farmland. *Yingyong Shengtai Xuebao* **2011**, *22*, 1261–1267.
8. Ramos, M.C.; Cots-Folch, R.; Martínez-Casasnovas, J.A. Effects of land terracing on soil properties in the Priorat region in Northeastern Spain: A multivariate analysis. *Geoderma* **2007**, *142*, 251–261. [CrossRef]
9. Tarolli, P.; Preti, F.; Romano, N. Terraced landscapes: From an old best practice to a potential hazard for soil degradation due to land abandonment. *Anthropocene* **2014**, *6*, 10–25. [CrossRef]
10. Arévalo, J.R.; Tejedor, M.; Jiménez, C.; Reyes-Betancort, J.A.; Díaz, F.J. Plant species composition and richness in abandoned agricultural terraces vs. natural soils on Lanzarote (Canary Islands). *J. Arid Environ.* **2016**, *124*, 165–171. [CrossRef]
11. Gravagnuolo, A.; Varotto, M. Terraced Landscapes Regeneration in the Perspective of the Circular Economy. *Sustainability* **2021**, *13*, 4347. [CrossRef]
12. Jiao, Y.; Yang, Y.; Hu, W.; Su, S. Analysis of the landscape pattern and aesthetic characteristics of the Hani terraced fields. *Geogr. Res.* **2006**, *4*, 624–632.
13. Varotto, M.; Bonardi, L.; Tarolli, P. *World Terraced Landscapes: History, Environment, Quality of Life*; Springer: Berlin/Heidelberg, Germany, 2018; Volume 9.
14. Terkenli, T.S.; Castiglioni, B.; Cisani, M. The challenge of tourism in terraced landscapes. In *World Terraced Landscapes: History, Environment, Quality of Life*; Springer: Berlin/Heidelberg, Germany, 2019; pp. 295–309.
15. Van Dijk, A.; Bruijnzeel, L.; Wiegman, S. Measurements of rain splash on bench terraces in a humid tropical steepland environment. *Hydrol. Process.* **2003**, *17*, 513–535. [CrossRef]
16. Díaz, A.R.; Sanleandro, P.M.; Soriano, A.S.; Serrato, F.B.; Faulkner, H. The causes of piping in a set of abandoned agricultural terraces in southeast Spain. *Catena* **2007**, *69*, 282–293. [CrossRef]
17. Lesschen, J.P.; Cammeraat, L.H.; Nieman, T. Erosion and terrace failure due to agricultural land abandonment in a semi-arid environment. *Earth Surf. Process. Landf.* **2008**, *33*, 1574–1584. [CrossRef]
18. Stavi, I.; Gusarov, Y.; Halbac-Cotoara-Zamfir, R. Collapse and failure of ancient agricultural stone terraces: On-site geomorphic processes, pedogenic mechanisms, and soil quality. *Geoderma* **2019**, *344*, 144–152. [CrossRef]
19. Kizos, T.; Dalaka, A.; Petanidou, T. Farmers' attitudes and landscape change: Evidence from the abandonment of terraced cultivations on Lesvos, Greece. *Agric. Hum. Values* **2010**, *27*, 199–212. [CrossRef]
20. Martínez-Casasnovas, J.A.; Ramos, M.C.; Cots-Folch, R. Influence of the EU CAP on terrain morphology and vineyard cultivation in the Priorat region of NE Spain. *Land Use Policy* **2010**, *27*, 11–21. [CrossRef]
21. Moreno-de-las-Heras, M.; Lindenberger, F.; Latron, J.; Lana-Renault, N.; Llorens, P.; Arnáez, J.; Romero-Díaz, A.; Gallart, F. Hydro-geomorphological consequences of the abandonment of agricultural terraces in the Mediterranean region: Key controlling factors and landscape stability patterns. *Geomorphology* **2019**, *333*, 73–91. [CrossRef]
22. Wen, Y.; Kasielke, T.; Li, H.; Zhang, B.; Zepp, H. May agricultural terraces induce gully erosion? A case study from the Black Soil Region of Northeast China. *Sci. Total Environ.* **2021**, *750*, 141715. [CrossRef]
23. Paliaga, G.; Luino, F.; Turconi, L.; De Graff, J.V.; Faccini, F. Terraced landscapes on Portofino Promontory (Italy): Identification, geo-hydrological hazard and management. *Water* **2020**, *12*, 435. [CrossRef]
24. Cicinelli, E.; Caneva, G.; Savo, V. A Review on Management Strategies of the Terraced Agricultural Systems and Conservation Actions to Maintain Cultural Landscapes around the Mediterranean Area. *Sustainability* **2021**, *13*, 4475. [CrossRef]
25. Sabir, M. The Terraces of the Anti-Atlas: From Abandonment to the Risk of Degradation of a Landscape Heritage. *Water* **2021**, *13*, 510. [CrossRef]
26. Fu, B.; Wang, S.; Liu, Y.; Liu, J.; Liang, W.; Miao, C. Hydrogeomorphic Ecosystem Responses to Natural and Anthropogenic Changes in the Loess Plateau of China. *Annu. Rev. Earth Planet. Sci.* **2017**, *45*, 223–243. [CrossRef]
27. Liu, X.; He, B.; Li, Z.; Zhang, J.; Wang, L.; Wang, Z. Influence of land terracing on agricultural and ecological environment in the loess plateau regions of China. *Environ. Earth Sci.* **2011**, *62*, 797–807. [CrossRef]

28. An, P.; Inoue, T.; Zheng, M.; Eneji, A.E.; Inanaga, S. Agriculture on the loess plateau. In *Restoration and Development of the Degraded Loess Plateau, China*; Springer: Berlin/Heidelberg, Germany, 2014; pp. 61–74.
29. Fu, B. Soil erosion and its control in the Loess Plateau of China. *Soil Use Manag.* **1989**, *5*, 76–82. [CrossRef]
30. Gao, H.; Li, Z.; Li, P.; Jia, L.; Zhang, X. Quantitative study on influences of terraced field construction and check-dam siltation on soil erosion. *J. Geogr. Sci.* **2012**, *22*, 946–960. [CrossRef]
31. Fu, B.; Chen, L.; Qiu, Y.; Wang, J.; Meng, Q. *Land Use Structure and Ecological Processes in the Loess Hilly Area, China*; Commercial Press: Beijing, China, 2002.
32. Feng, Z.; Yang, Y.; Zhang, Y.; Zhang, P.; Li, Y. Grain-for-green policy and its impacts on grain supply in West China. *Land Use Policy* **2005**, *22*, 301–312. [CrossRef]
33. Li, L.; Tonts, M. The impacts of temporary labour migration on farming systems of the Loess Plateau, Gansu Province, China. *Popul. Space Place* **2014**, *20*, 316–332. [CrossRef]
34. Tsunekawa, A.; Liu, G.; Yamanaka, N.; Du, S. *Restoration and Development of the Degraded Loess Plateau, China*; Springer: Berlin/Heidelberg, Germany, 2014.
35. Wei, J.-Z.; Zheng, K.; Zhang, F.; Fang, C.; Zhou, Y.-Y.; Li, X.-C.; Li, F.-M.; Ye, J.-S. Migration of rural residents to urban areas drives grassland vegetation increase in China's Loess Plateau. *Sustainability* **2019**, *11*, 6764. [CrossRef]
36. Cao, S.; Xu, C.; Chen, L.; Wang, X. Attitudes of farmers in China's northern Shaanxi Province towards the land-use changes required under the Grain for Green Project, and implications for the project's success. *Land Use Policy* **2009**, *26*, 1182–1194. [CrossRef]
37. Fu, B.; Liu, Y.; Lü, Y.; He, C.; Zeng, Y.; Wu, B. Assessing the soil erosion control service of ecosystems change in the Loess Plateau of China. *Ecol. Complex.* **2011**, *8*, 284–293. [CrossRef]
38. Lü, Y.; Fu, B.; Feng, X.; Zeng, Y.; Liu, Y.; Chang, R.; Sun, G.; Wu, B. A policy-driven large scale ecological restoration: Quantifying ecosystem services changes in the Loess Plateau of China. *PLoS ONE* **2012**, *7*, e31782. [CrossRef]
39. Dong, X.; Wang, X.; Wei, H.; Fu, B.; Wang, J.; Uriarte-Ruiz, M. Trade-offs between local farmers' demand for ecosystem services and ecological restoration of the Loess Plateau, China. *Ecosyst. Serv.* **2021**, *49*, 101295. [CrossRef]
40. Tsermegas, I.; Ewski, M.; Biejat, K.; Szynkiewicz, A. Function of Agricultural Terraces in Mediterranean Conditions-Selected Examples From the Island of Ikaria (The Southern Sporades, Greece). *Misc. Geogr.-Reg. Stud. Dev.* **2011**, *15*, 65–78. [CrossRef]
41. Brandolini, P.; Cevasco, A.; Capolongo, D.; Pepe, G.; Lovergine, F.; Del Monte, M. Response of terraced slopes to a very intense rainfall event and relationships with land abandonment: A case study from Cinque Terre (Italy). *Land Degrad. Dev.* **2018**, *29*, 630–642. [CrossRef]
42. Liu, K.; Ding, H.; Tang, G.; Na, J.; Huang, X.; Xue, Z.; Yan, X.; Li, F. Detection of Catchment-Scale Gully-Affected Areas Using Unmanned Aerial Vehicle (UAV) on the Chinese Loess Plateau. *Int. J. Geo-Inf.* **2016**, *5*, 238. [CrossRef]
43. d'Oleire-Oltmanns, S.; Marzolff, I.; Peter, K.D.; Ries, J.B. Unmanned aerial vehicle (UAV) for monitoring soil erosion in Morocco. *Remote Sens.* **2012**, *4*, 3390–3416. [CrossRef]
44. Xiong, L.; Tang, G.; Yang, X.; Li, F. Geomorphology-oriented digital terrain analysis: Progress and perspectives. *J. Geogr. Sci.* **2021**, *31*, 456–476. [CrossRef]
45. Colomina, I.; Molina, P. Unmanned aerial systems for photogrammetry and remote sensing: A review. *ISPRS J. Photogramm. Remote Sens.* **2014**, *92*, 79–97. [CrossRef]
46. Pijl, A.; Quarella, E.; Vogel, T.A.; D'Agostino, V.; Tarolli, P. Remote sensing vs. field-based monitoring of agricultural terrace degradation. *Int. Soil Water Conserv. Res.* **2021**, *9*, 1–10. [CrossRef]
47. Ressl, C.; Brockmann, H.; Mandlburger, G.; Pfeifer, N. Dense Image Matching vs. Airborne Laser Scanning—Comparison of two methods for deriving terrain models. *Photogramm.-Fernerkund.-Geoinf.* **2016**, *2016*, 57–73. [CrossRef]
48. Manfreda, S.; McCabe, M.F.; Miller, P.E.; Lucas, R.; Pajuelo Madrigal, V.; Mallinis, G.; Ben Dor, E.; Helman, D.; Estes, L.; Ciraolo, G. On the use of unmanned aerial systems for environmental monitoring. *Remote Sens.* **2018**, *10*, 641. [CrossRef]
49. Na, J.; Xue, K.; Xiong, L.; Tang, G.; Pfeifer, N. UAV-Based Terrain Modeling under Vegetation in the Chinese Loess Plateau: A Deep Learning and Terrain Correction Ensemble Framework. *Remote Sens.* **2020**, *12*, 3318. [CrossRef]
50. Aplin, P.; Smith, G.M. Introduction to object-based landscape analysis. *Int. J. Geogr. Inf. Sci.* **2011**, *25*, 869–875. [CrossRef]
51. Blaschke, T. Object based image analysis for remote sensing. *ISPRS J. Photogramm. Remote Sens.* **2010**, *65*, 2–16. [CrossRef]
52. Zhao, H.; Fang, X.; Ding, H.; Josef, S.; Xiong, L.; Na, J.; Tang, G. Extraction of terraces on the Loess Plateau from high-resolution DEMs and imagery utilizing object-based image analysis. *ISPRS Int. J. Geo-Inf.* **2017**, *6*, 157. [CrossRef]
53. Blaschke, T.; Strobl, J. What's wrong with pixels? Some recent developments interfacing remote sensing and GIS. *Z. Geoinf.* **2015**, *6*, 12–17.
54. Frohn, R.C.; Autrey, B.C.; Lane, C.R.; Reif, M. Segmentation and object-oriented classification of wetlands in a karst Florida landscape using multi-season Landsat-7 ETM+imagery. *Int. J. Remote Sens.* **2011**, *32*, 1471–1489. [CrossRef]
55. Liu, K.; Ding, H.; Tang, G.; Zhu, A.X.; Yang, X.; Sheng, J.; Cao, J. An object-based approach for two-level gully feature mapping using high-resolution DEM and imagery: A case study on hilly loess plateau region, China. *Chin. Geogr. Sci.* **2017**, *27*, 415–430. [CrossRef]
56. Na, J.; Ding, H.; Zhao, W.; Liu, K.; Tang, G.; Pfeifer, N. Object-based large-scale terrain classification combined with segmentation optimization and terrain features: A case study in China. *Trans. GIS* **2021**. [CrossRef]

57. Malinverni, E.S.; Tassetti, A.N.; Mancini, A.; Zingaretti, P.; Frontoni, E.; Bemardini, A. Hybrid object-based approach for land use/land cover mapping using high spatial resolution imagery. *Int. J. Geogr. Inf. Ence* **2011**, *25*, 1025–1043. [CrossRef]
58. Rau, J.Y.; Hsiao, K.W.; Jhan, J.P.; Wang, S.H.; Wang, J.L. Bridge crack detection using multi-potary UAV and object-based image analysis. *ISPRS-Int. Arch. Photogramm. Remote Sens. Spat. Inf. Sci.* **2017**, *XLII-2/W6*, 311–318. [CrossRef]
59. Wouters, L.; Moel, H.D.; Ruiter, M.D.; Couasnon, A.; Teklesadik, A. Improving flood damage assessments in data-scarce areas by retrieving building characteristics through automated UAV image processing. In Proceedings of the Advances in Geomatics Research Conference (AGRC2019), Kampala, Uganda, 1–2 August 2019.
60. Boonpook, W.; Tan, Y.; Xu, B. Deep learning-based multi-feature semantic segmentation in building extraction from images of UAV photogrammetry. *Int. J. Remote Sens.* **2021**, *42*, 1–19. [CrossRef]
61. Burdziakowski, P.; Specht, C.; Dabrowski, P.S.; Specht, M.; Lewicka, O.; Makar, A. Using UAV photogrammetry to analyse changes in the coastal zone based on the sopot tombolo (Salient) measurement project. *Sensors* **2020**, *20*, 4000. [CrossRef]
62. Som-Ard, J.; Hossain, M.; Ninsawat, S.; Veerachitt, V. Pre-harvest Sugarcane Yield Estimation Using UAV-Based RGB Images and Ground Observation. *Sugar Tech* **2018**, *20*, 645–657. [CrossRef]
63. Comert, R.; Avdan, U.; Gorum, T.; Nefeslioglu, H.A. Mapping of shallow landslides with object-based image analysis from unmanned aerial vehicle data. *Eng. Geol.* **2019**, *260*, 105264. [CrossRef]
64. Karantanellis, E.; Marinos, V.; Vassilakis, E. 3D Hazard analysis and object-based characterization of landslide motion mechanism using UAV imagery. *Int. Arch. Photogramm. Remote Sens. Spat. Inf. Sci.* **2019**, *42(2W/13)*, 425–430. [CrossRef]
65. Rossi, G.; Tanteri, L.; Tofani, V.; Vannocci, P.; Casagli, N. Multitemporal UAV surveys for landslide mapping and characterization. *Landslides* **2018**, *15*, 1045–1052. [CrossRef]
66. Ding, H.; Na, J.; Jiang, S.; Zhu, J.; Li, F. Evaluation of Three Different Machine Learning Methods for Object-Based Artificial Terrace Mapping—A Case Study of the Loess Plateau, China. *Remote Sens.* **2021**, *13*, 1021. [CrossRef]
67. Huang, C.; Yang, Q.; Cao, X.; Li, Y. Assessment of the Soil Erosion Response to Land Use and Slope in the Loess Plateau—A Case Study of Jiuyuangou. *Water* **2020**, *12*, 529. [CrossRef]
68. Baatz, M.; Schape, A. Multiresolution segmentation: An optimization approach for high quality multi-scale image segmentation. *Angew. Geogr. Inf.* **2000**.
69. Drăguţ, L.; Tiede, D.; Levick, S.R. ESP: A tool to estimate scale parameter for multiresolution image segmentation of remotely sensed data. *Int. J. Geogr. Inf. Sci.* **2010**, *24*, 859–871. [CrossRef]
70. Ding, H.; Liu, K.; Chen, X.; Xiong, L.; Strobl, J. Optimized Segmentation Based on the Weighted Aggregation Method for Loess Bank Gully Mapping. *Remote Sens.* **2020**, *12*, 793. [CrossRef]
71. Li, S.; Xiong, L.; Tang, G.; Strobl, J. Deep learning-based approach for landform classification from integrated data sources of digital elevation model and imagery. *Geomorphology* **2020**, *354*, 107045. [CrossRef]
72. Belgiu, M.; Dragut, L. Random forest in remote sensing: A review of applications and future directions. *ISPRS J. Photogramm.* **2016**, *114*, 24–31. [CrossRef]
73. Gómez-Gutiérrez, Á.; Conoscenti, C.; Angileri, S.E.; Rotigliano, E.; Schnabel, S. Using topographical attributes to evaluate gully erosion proneness (susceptibility) in two mediterranean basins: Advantages and limitations. *Nat. Hazards* **2015**, *79*, 291–314. [CrossRef]
74. Haralick, R.M.; Shanmugam, K.; Dinstein, I.H. Textural features for image classification. *IEEE Trans. Syst. Man Cybern.* **1973**, *6*, 610–621. [CrossRef]
75. Woebbecke, D.M.; Meyer, G.E.; Von Bargen, K.; Mortensen, D.A. Color indices for weed identification under various soil, residue, and lighting conditions. *Trans. ASAE* **1995**, *38*, 259–269. [CrossRef]
76. Burrough, P.A.; McDonnell, R.A.; McDonnell, R.; Lloyd, C.D. *Principles of Geographical Information Systems*; Oxford University Press: Oxford, UK, 2015.
77. d'Oleire-Oltmanns, S.; Eisank, C.; Drăgut, L.; Blaschke, T. An object-based workflow to extract landforms at multiple scales from two distinct data types. *IEEE Geosci. Remote Sens. Lett.* **2013**, *10*, 947–951. [CrossRef]
78. Shruthi, R.B.; Kerle, N.; Jetten, V. Object-based gully feature extraction using high spatial resolution imagery. *Geomorphology* **2011**, *134*, 260–268. [CrossRef]
79. Shruthi, R.B.; Kerle, N.; Jetten, V.; Stein, A. Object-based gully system prediction from medium resolution imagery using Random Forests. *Geomorphology* **2014**, *216*, 283–294. [CrossRef]
80. Shafer, G. *A Mathematical Theory of Evidence*; Princeton University Press: Princeton, NJ, USA, 1976.
81. Mezaal, M.R.; Pradhan, B.; Rizeei, H.M. Improving landslide detection from airborne laser scanning data using optimized Dempster–Shafer. *Remote Sens.* **2018**, *10*, 1029. [CrossRef]
82. Summerfield, M. Sub-aerial denudation of passive margins: Regional elevation versus local relief models. *Earth Planet. Sci. Lett.* **1991**, *102*, 460–469. [CrossRef]
83. Bohlin, J.; Wallerman, J.; Fransson, J.E. Forest variable estimation using photogrammetric matching of digital aerial images in combination with a high-resolution DEM. *Scand. J. For. Res.* **2012**, *27*, 692–699. [CrossRef]
84. Lucieer, A.; Jong, S.M.d.; Turner, D. Mapping landslide displacements using Structure from Motion (SfM) and image correlation of multi-temporal UAV photography. *Prog. Phys. Geogr.* **2014**, *38*, 97–116. [CrossRef]
85. El Bastawesy, M.; Cherif, O.; Sultan, M. The geomorphological evidences of subsidence in the Nile Delta: Analysis of high resolution topographic DEM and multi-temporal satellite images. *J. Afr. Earth Sci.* **2017**, *136*, 252–261. [CrossRef]

86. Schilling, K.E.; Jacobson, P.J. Water and nutrient discharge to a high-value terrace–floodplain fen: Resilience and risk. *Ecohydrology* **2016**, *9*, 1196–1207. [CrossRef]
87. Gibson, C.A.; Koch, B.J.; Compson, Z.G.; Hungate, B.A.; Marks, J.C. Ecosystem responses to restored flow in a travertine river. *Freshw. Sci.* **2018**, *37*, 169–177. [CrossRef]
88. Shrestha, D.; Zinck, J.; Van Ranst, E. Modelling land degradation in the Nepalese Himalaya. *Catena* **2004**, *57*, 135–156. [CrossRef]
89. Ma, H.; Li, J.; He, X.; Liu, X.; Wang, F. The status and sediment reduction effects of level terrace in the Loess Plateau. *Yellow River* **2015**, *37*, 89–93. (In Chinese)
90. Guo, J.; He, L.; Pei, Z.; Lv, D.; Lei, S.; Zhang, X. Investigation and Analysis of Damage of Horizontal Terraced Fields Under Extreme Rainstorm Conditions in the Loess Plateau—Taking the 7.26 Torrential Rain in the Chabagou Watershed as an Example. *Res. Soil Water Conserv.* **2019**, *26*, 111–117. (In Chinese)